Brain-wide measurement of protein turnover with high spatial and temporal resolution

Boaz Mohar[1], Jonathan B. Grimm[1], Ronak Patel[1], Timothy A. Brown[1], Paul W. Tillberg[1], Luke D. Lavis[1], Nelson Spruston[1], Karel Svoboda[1,2]

[1]Janelia Research Campus, Howard Hughes Medical Institute, Ashburn, VA, USA

[2]Allen Institute for Neural Dynamics, Seattle, WA, USA

ABSTRACT

Cellular functions are regulated by synthesizing and degrading proteins on time scales ranging from minutes to weeks. Protein turnover varies across proteins, cellular compartments, cell types, and tissues. In the brain, circuit-specific protein turnover is thought to underlie synaptic plasticity, but current methods to track protein turnover lack cellular or subcellular resolution. We describe a pulse–chase method (DELTA) to measure protein turnover with high spatial and temporal resolution throughout the body. DELTA relies on the rapid covalent capture by HaloTag of fluorescent ligands optimized for bioavailability *in vivo*, overcoming the unique challenges associated with labeling in the brain. We found that the nuclear protein MeCP2 showed brain-region- and cell-type-specific turnover, and the synaptic protein PSD95 was destabilized in specific brain regions following behavioral enrichment. A new variant of

expansion microscopy enabled turnover measurements at individual synapses. DELTA will enable studies of adaptive and maladaptive plasticity in brain-wide neural circuits.

INTRODUCTION

Cellular functions are regulated by tuning protein synthesis and degradation, which results in dynamic protein turnover[1–3] in the range of hours to days[4]. In the brain, protein lifetimes range from tens of minutes for immediate early gene proteins[5] to months for some synaptic structural proteins[6]. Turnover rates vary by protein location or function, cell type, and brain region[7–9]. Protein dynamics also depend on environmental and behavioral conditions[9,10] and are disrupted in neurodegenerative diseases[11]. Protein turnover is necessary to learn cognitive and motor tasks[12–14]. For example, learning is supported by long-term changes in synaptic strength that require both protein synthesis[15,16] and degradation[17–19]. During learning and behavior, activity-dependent gene regulation occurs throughout brain-wide neural circuits[20–22], but changes in synaptic strength are limited to active synapses[23–27], suggesting subcellular regulation of protein turnover. This combination of brain-wide and subcellular regulation calls for multiscale measurements of protein turnover *in vivo*.

Metabolic incorporation of modified amino acids followed by mass spectrometry (MS) allows the measurement of turnover for many proteins in parallel[28], but spatial resolution is limited to the level of brain regions (*e.g.*, cortex *vs.* cerebellum) or homogenate fractions (*e.g.*, cytoplasm *vs.* synaptosomes). Furthermore, results vary between individual studies depending on the cellular fraction selected and other experimental conditions (*e.g.*, *in vitro vs. in vivo*; for a review see Alvarez-Castelao & Schuman[29]), exhibiting considerable variability for any single protein, making comparisons across animals and studies difficult. Alternatively, fluorescent imaging methods allow for labeling with different fluorophores at specific time points by fusing

a tag with a protein of interest. This approach offers better spatial resolution, but remains difficult to deploy in the brain due to issues with epitope tags and labeled antibodies[30,31]. Tracking brain turnover is also an issue for the self-labeling SNAP-tag[32] system and cognate ligands that do not cross the blood-brain barrier[33,34]. Recently, the HaloTag[35] system (another self-labeling enzymatic tag) was used with a single fluorescent ligand (pulse-only) to image protein turnover at high spatial resolution in the brain[36]. But this pulse-only protocol requires pooling data across different animals, limiting the precision of the method.

We overcome these issues by using the HaloTag system with multiple fluorescent ligands in a pulse–chase protocol. We first used simulations and *in vivo* calibration measurements to assess the sensitivity and precision of pulse–chase experiments, showing them to be superior to pulse-only measurements. We then identified a panel of Janelia Fluor (JF) dyes attached to the HaloTag ligand[37–39] that are optimized for bioavailability *in vivo*, including in the brain. These JF dye-HaloTag ligands are available to the scientific community[40]. Using spectrally separable dyes, we developed a robust pulse–chase protocol to estimate protein lifetimes *in vivo*—a method we named DELTA (**D**ye **E**stimation of the **L**ifetime of pro**T**eins in the br**A**in). DELTA enabled precise measurements of protein lifetime in the whole brain and other tissues *in vivo*, down to synaptic resolution, even for synapses with low levels of synaptic protein. We used DELTA with the HaloTag protein fused to the nuclear transcriptional repressor protein MeCP2 and the synaptic scaffold protein PSD95, and we measured the brain-wide protein turnover of these proteins at subcellular resolution.

RESULTS

Measuring protein turnover *in vivo* with high spatial and temporal resolution. We first modeled the dye labeling process *in vivo* to identify the conditions where a pulse–chase method would enable precise protein turnover measurements. We defined three populations of HaloTag fusion proteins (**Fig. 1a**): *Unlabeled* protein–HaloTag; *Pulse*, the population labeled with the first dye infusion; and *Chase*, the population synthesized after the first dye cleared and labeled with a spectrally distinct dye. Assuming exponential decay of proteins, we can calculate their mean lifetime $\tau = \Delta t/\log(1/\textit{Fraction Pulse})$, where Δt is the time interval between pulse and chase dye administration and *Fraction Pulse* is the proportion of protein-HaloTag fusion labeled by the pulse dye ($\textit{Fraction Pulse} = \textit{Pulse}/[\textit{Pulse} + \textit{Chase}]$). We noticed that the rate of dye clearance limits the time resolution of turnover measurements (**Fig. 1a-**gray shaded region**; Supplementary Note 1**). *In vivo* fluorescence imaging determined a time constant of approximately 82 min for dye clerance (**Extended Data Fig. 1**).

With this framework and data in hand, we investigated the effects of the three variables: the selection of target protein, through its mean lifetime; the amount of dye injected, which determines ligand to target ratio; and the pulse-chase interval (Δt; **Fig. 1b, Extended Data Fig. 2**, **Supplementary Note 1**). We find that underlabeling produces large errors in estimated lifetime, regardless of true protein lifetime, while ligand excess produced only small errors over a broad range of lifetime values, except for proteins where lifetime ≤ dye clearance (**Fig. 1b**). Given that most proteins in the brain have longer lifetimes[1,9] than dye clearance, ligand excess will allow accurate turnover measurements. Additionally, errors produced by ligand excess would not distort relative measurements of protein lifetime across cell types, brain regions, or individual animals. We then compared DELTA (a pulse–chase method) to using a single dye

(*i.e.*, pulse-only)[36]. The pulse-only protocol is sensitive to variability in protein concentrations and imaging conditions across animals, causing potentially large errors in turnover estimates (**Extended Data Fig. 2g**) reduced only by averaging across many animals. The chase ligand normalizes these parameters and increases the signal-to-noise ratio for imaging later time points (SNR; **Extended Data Fig. 2h**).

This pulse–chase protocol requires spectrally distinct dyes that efficiently bind HaloTag fusion proteins *in vivo*. We screened the bioavailability of JF HaloTag ligands[37–39] in mouse brains. We expressed fluorescent protein fused to HaloTag (GFP-HaloTag or mKate2-HaloTag) and administered a pulse dye retro-orbitally followed by perfusion of the brain with a different chase dye after 12–18 hours. Under these conditions, the unbound pulse dye clears while protein degradation and synthesis are minimal[41], so higher chase dye signal indicates lower bioavailability of the pulse ligand. This experiment identified JF_{669}-HaloTag ligand and JF_{552}-HaloTag ligand as particularly bioavailable, with both dyes producing strong and uniform labeling across the brain (**Extended Data Fig. 3**, **Supplementary Note 2**).

Measuring cell type and brain region-specific turnover of the nuclear protein MeCP2. We used DELTA to measure the lifetime of methyl-CpG binding protein 2 (MeCP2), an abundant nuclear protein implicated in chromatin remodeling in neurons, and in Rett syndrome[42–44]. We measured MeCP2 turnover by applying DELTA in MeCP2–HaloTag knock-in mice[45]. Previous MeCP2 lifetime measurements using metabolic pulse–chase labeling provide a point of comparison for our method[9]. To assess saturation, we injected JF_{669}-HaloTag ligand retro-orbitally (*Pulse*), followed by perfusion with JF_{585}-HaloTag ligand (*Chase*) after 1 h (**Extended Data Fig. 4a**). The lack of *Chase* indicated saturation with the pulse dye ligand in almost all tissues, including most regions of the brain (**Extended Data Fig. 4b–h**). Some brain

regions containing dense cell body layers were not saturated, including the hippocampal CA1 region and Dentate Gyrus (**Extended Data Fig. 4i**, **Supplementary Note 2**). Nuclei located furthest from the vasculature exhibited lower labeling intensities, suggesting this is due to ligand depletion in regions with densely clustered nuclei expressing large amounts[46] of MeCP2–HaloTag (top 95th percentile of proteins in the brain). Nevertheless, we achieved MeCP2–HaloTag saturation in most brain regions. This depletion issue is less pertinent for cytosolic, dendritic, and axonal proteins, which are expected to be more homogeneously distributed with respect to vasculature.

To make turnover measurements more precise and compile multiple estimates of protein lifetime from the same animal, we sequentially injected the highly bioavailable dyes JF_{669}-HaloTag ligand and JF_{552}-HaloTag ligand, followed by perfusion of a third dye: JF_{608}-HaloTag ligand, which is less bioavailable but penetrates the brain during perfusion. After perfusion, the brain was sectioned and stained with DAPI to identify all nuclei, and immunofluorescence (IF) was used to classify cell types (**Fig. 1c**). We imaged the JF_{669}-HaloTag ligand, JF_{608}-HaloTag ligand, and JF_{552}-HaloTag ligand fluorescence with subcellular resolution and calculated *Fraction Pulse* for all neuronal nuclei across the brain of five MeCP2–HaloTag mice. We segmented MeCP2 nuclei and converted the measurements to average protein lifetime (τ) under the assumption of single exponential decay (**Fig. 1d,e**). The lifetime of MeCP2 differed across brain regions (**Fig. 1f**). To assess the consistency of our method, we looked at pairwise correlations across animals for all commonly imaged brain regions. The average mean correlation across pairs was high compared to shuffled controls for three levels of region annotation representing different spatial scales based on the Allen Brain Reference common coordinate framework (CCFv3; **Extended Data Fig. 5a–c**)[47]. The lifetime of MeCP2 was

longest in the cerebellum (**Fig. 1e**, right panel), in agreement with previous work using mass spectrometry (MS)[9].

We also compared MeCP2 in neuronal and non-neuronal cells. Consistent with previous studies[48], we found that MeCP2 is expressed at higher levels in neurons (**Extended Data Fig. 5d,e**). Within the same cortical region, we observed similar lifetimes of MeCP2–HaloTag in neurons, oligodendrocytes, and microglia (**Extended Data Fig. 5f**). This contrasts with a previous study comparing neuronal and non-neuronal cells throughout the brain[9], which found that non-neuronal MeCP2 had a longer lifetime than neuronal MeCP2. These results highlight the benefits of our pulse–chase paradigm, as it enables measurements of protein lifetime in subcellular compartments and at brain-wide scales.

PSD95 turnover is accelerated by behavioral enrichment. We next investigated the brain-wide dynamics of PSD95, a synaptic scaffold protein abundant in postsynaptic densities of excitatory synapses[49], using knock-in mice expressing PSD95 fused with HaloTag[50]. To facilitate the measurement of protein lifetimes in individual synapses, we developed an improved dye ligand: JFX_{673}-HaloTag ligand (**Fig. 2a**, **Extended Data Fig. 6**). This dye is structurally similar to JF_{669}-HaloTag ligand, but has deuterated pyrrolidine substituents instead of azetidines, which improves fluorophore brightness and photostability[39]. This novel dye retained the high bioavailability of its parent JF_{669} ligand[38] and saturated the HaloTag protein in the PSD95–HaloTag knock-in mouse line (**Extended Data Fig. 7a,b**). We also confirmed that JFX_{673} label colocalized with an antibody stain against PSD95 (**Extended Data Fig. 7c).**

We measured the lifetime of PSD95–HaloTag and the effects of behavioral manipulations (**Fig. 2b**), using dye injection formulations optimized to saturate the HaloTag fusion (**Supplementary Note 3**). Control mice (n = 2) and mice placed in an enriched environment (EE;

n = 4)[51,52] were imaged with a pulse–chase interval of 14 days using JFX_{673}-HaloTag ligand as the pulse dye and JF_{552}-HaloTag ligand as the chase dye. Following imaging (**Fig. 2c,d**), sections were registered to the Allen Brain Reference (CCFv3), and the lifetime of PSD95 was calculated (**Fig. 2e**). Both Control and EE groups showed variations in PSD95–HaloTag lifetime (τ) in different brain regions, such as different cortical layers or hippocampal subfields (**Fig. 2f,g**). We observed significant differences across the twelve main brain regions (**Fig. 2h**). Both the brain regions and layer differences were consistent across individual animals (**Extended Data Fig. 7d**).

We assessed the variability across animals in total PSD95 signal (*Pulse+Chase*) as we expected it to be lower using DELTA compared to a pulse-only method (**Extended Data Fig. 2g**). Indeed, the coefficient of variation across animals was around 2× lower in DELTA than a previously published[36] pulse-only method (**Extended Data Fig. 7e)**. Our computational model also predicts a correlation between the expression intensity and turnover in a pulse-only method due to lower SNR (**Extended Data Fig. 2h**). This prediction is indeed evident in pulse-only data but not in DELTA (**Extended Data Fig. 7f, g**). Lastly, we did not see a correlation between turnover rates and proximity to brain vasculature[53]. For example, in both the hippocampus and neocortex, most blood vessels are oriented dorsoventrally while the variation of turnover is mediolateral in the hippocampus (CA1 *vs.* CA3) and dorsoventral in neocortex (Layer 1 to Layer 6; **Fig. 2e,f**). This provides a good test case for biases that could arise from inhomogeneous delivery of ligands via the vasculature as PSD95-HaloTag signal is homogenous at this resolution.

Averaging across all brain regions, the brain-wide average half-life of PSD95 was more than a day, or ~10% shorter, in mice housed for two weeks in EE compared with standard housed

controls (**Fig. 2i**). To determine whether EE modulates lifetime preferentially in some regions over others, we compared the differences between EE and Control animals across brain regions. We observed that the neocortex had the largest difference (**Fig. 2j**). We then examined finer-scale regions, namely different neocortical layers and subfields of the hippocampus. At this spatial resolution, the mean lifetime and effects of EE on lifetime exhibit smooth variation across neocortical layers, but in different patterns. For example, layer 1 had the longest PSD95–HaloTag lifetime, whereas PSD95–HaloTag was maximally destabilized in layer 4 after EE (**Fig. 2k**).

Individual synapses are thought to form the basis of learning in the brain[26]. Investigating PSD95–HaloTag turnover in individual synapses requires an approximately four-fold higher resolution than permitted by the diffraction limit. Expansion microscopy (ExM)[54] allows for this four-fold enhancement, but uniform expansion requires dissolving the native tissue structure through proteolysis or strong denaturation, leading to loss of signal (~50% for antibodies or fluorescent proteins)[55]. We developed an ExM protocol that enables two-fold expansion without proteolysis or strong protein denaturation. We imaged the expanded sample with Airyscan confocal microscopy[56], which provides another two-fold improvement in resolution, yielding the required four-fold improvement. This approach, combined with our use of bright and photostable small-molecule dyes, enabled measurements of turnover at individual synapses. We applied this method to different brain regions of one coronal section and were able to measure the turnover in single synapses of cortical layer 1 and CA1, both of which had longer lifetimes than CA3 synapses (**Fig. 2l**; **Supplementary Movie 3**, **4**). This shows that DELTA combines brain-wide coverage with single-synapse resolution and sensitivity.

DISCUSSION

Through modeling, calibration measurements, and screening of dye ligands we developed a robust pulse–chase method, DELTA, that enables the measurement of protein lifetime with high temporal and spatial precision. We defined the appropriate conditions for implementing this pulse–chase procedure in the mouse brain. We also introduced a new dye, JFX_{673}-HaloTag ligand, with improved photophysical properties and excellent pharmacokinetics in the brain. Consistent with previous measurements using metabolic labeling, we found that MeCP2–HaloTag protein turnover is slower in the cerebellum compared to other areas of the brain; both measurements also gave a lifetime of around 11 days for other brain regions. We then measured the lifetime of the major excitatory synaptic scaffold protein PSD95 over a range of spatial scales from brain regions to single synapses. We found that PSD95–HaloTag lifetimes ranged from 11–14 days depending on brain region. This is in line with previous measurements of PSD95 lifetime measured by metabolic labeling and mass spectrometry (MS, 11-16 days[9]; but see[1,6]). Finally, PSD95–HaloTag turnover is increased by enriched experience, with middle cortical layers and CA1 as major loci of plasticity.

DELTA complements MS-based methods for measuring protein lifetime. MS can measure 1000s of proteins in parallel but requires expensive, specialized equipment and provides low spatial resolution. DELTA only measures lifetime of one protein at a time but does so on spatial scales ranging from millimeters to ~100 nanometers by using modern histology and microscopy methods. DELTA requires genetic manipulation and dye saturation tests for each new knock-in mouse but is easily combined with other imaging-based molecular methods, such as fluorescence *in situ* hybridization (FISH)[57] or immunofluorescence (**Fig. 1d**). A key advantage of DELTA over pulse-only methods[36] is the use of the chase dye to normalize for variability across animals

(**Extended Data Fig. 2g**), which improves the precision of the method, especially with lower expressing proteins (**Extended Data Fig. 2h**; **Extended Data Fig. 7f,g**). With new transgenic mice expressing synaptic proteins fused to HaloTag (*e.g.*, GluA2-HaloTag), DELTA could be used to identify brain regions, neurons, and even subcellular compartments that undergo plasticity during learning.

Beyond measuring lifetime for other proteins and in other subcellular compartments, DELTA can be combined with the expression of indicators or actuators of neural activity to examine the relationship between neural activity and protein turnover. This could also be done in both healthy mice and animal models of neurological or psychiatric disorders. More sophisticated pulse–chase paradigms using additional dyes (**Fig. 1c**) or nonfluorescent HaloTag ligands[58,59] could be used to compare turnover in a control epoch and an experimental epoch in the same experiment. Overall, DELTA could help identify organ-wide changes involved in adaptive and maladaptive processes in an unbiased and high-throughput manner.

METHODS

Materials. Precommercial JF-HaloTag ligands are freely available from HHMI's Open Chemistry[40] initiative *via* dyes.janelia.org. Purified HaloTag protein (#G4491) was purchased from Promega. Pluronic F-127 (# P3000MP), anhydrous dimethylsulfoxide (DMSO; #D12345), *N*,*N*,*N′*,*N′*-tetramethylethylenediamine (TEMED; #15524010), ammonium persulfate (APS; #AAJ7632209), and acryloyl-X succinimidyl ester (AcX-SE; #A20770) were purchased from ThermoFisher Scientific. Acrylamide (#1610140) and bis-acrylamide (#1610142) were purchased from Bio-Rad (Hercules, CA). To prepare sodium acrylate for expansion microscopy experiments we neutralize acrylic acid purchased from TCI (#A0141) with sodium hydroxide as

previously described[60]. 4-Hydroxy-TEMPO (4HT; #176141) was purchased from Sigma (Saint Louis, MO).

Animals. All procedures were carried out according to protocols approved by the Janelia Institutional Animal Care and Use Committee (IACUC). Wild-type mice (C57Bl/6J RRID: IMSR_JAX:000664; both male and female) were housed in a 12:12 reverse light:dark cycle. MeCP2-HaloTag knock-in mice[45] and PSD95-HaloTag knock-in mice[50] of either sex were used.

Virus, dye injections, and tissue processing. Evaluation of the ability of different JF-HaloTag ligands to saturate HaloTag proteins in the brain requires expression of a HaloTag-labeled protein. For most JF dyes excited by light >550 nm we used HaloTag–EGFP. An mKate-HaloTag was used for JF_{525}-HaloTag ligand. Viruses and dye were delivered using retro-orbital (RO) injections. Viruses expressing HaloTag-EGFP or HaloTag-mKate2 used the PHP.eB AAV capsid[61] with a synapsin promoter. 100 µL of virus (titer of 4e11 GC/mL) was injected RO. RO dye injections (pulse) were performed 3–5 weeks after virus injection. Most injections were prepared by dissolving 100 nmol of dye in 20 µl DMSO followed by 20 µL of 20% Pluronic F-127 in DMSO and 60 µl of Phosphate Buffered Saline (PBS), except when otherwise noted (**Supplementary Note 2**; for dye preparation see DOI: 0.17504/protocols.io.5u4g6yw; for injection see DOI: 10.17504/protocols.io.5udg6s6). 24 hours after dye injection, animals were perfused with 50 mL of 4% PFA in 0.1 M sodium phosphate, pH 7.4 (phosphate buffer, PB) and 50 nmol of orthogonal dye (for tissue preparation see DOI: 10.17504/protocols.io.59jg94n). The brains were post-fixed in 4% PFA in 0.1 M PB overnight at 4 °C and washed three times in PBS for 15 minutes. 100 µm coronal sections were cut and floated in 24-well plates followed by 4 h of DAPI staining (0.6 µM in PBS) and washed 3 times for 15 minutes in PBS. For animals with

visible fluorescence from in vivo injection, every fourth slice was mounted for imaging; for animals where no fluorescence was observed, every 24th slice was mounted and imaged.

Immunofluorescence. For MeCP2-HaloTag animals, we preformed immunofluorescence (IF) staining to assign cell types to each nucleus (**Fig. 1c,d; Extended Data Fig. 5**). This was done on sequential coronal sections from each of the five animals. Briefly, after sectioning, sections were blocked in PBS with 2% BSA and 0.1% Triton X-100 for 1 h at room temperature. Primary antibodies (Rabbit Anti-NeuN RRID: AB_10807945; Rabbit Anti-Iba1 RRID: AB_2636859; Rabbit Anti-SOX10 RRID: AB_2721184) were used at 1:250 dilution in the same buffer as blocking overnight at 4 °C. Then, the sections were washed in the same buffer three times for 15 minutes. The sections were incubated with a Goat Anti-Rabbit AF488 secondary antibody (RRID: AB_143165) at 1:500 dilution for 24 h at 4 °C. After three more 15-min washes, the slices were stained with DAPI as described above and mounted. For PSD95 (**Extended Data Fig. 7c**), we used the knockout-validated anti-PSD95 antibody from NeuroMAB (RRID: AB_10807979) with a Goat Anti-Mouse CF633 secondary (RRID: AB_10854245).

Expansion Microscopy. After sectioning, coronal sections were anchored with AcX (0.033 mg/mL; 1:300 from 10 mg/mL stock in DMSO) in PBS for 1 h. Then they were moved to gelation solution containing: 2.7 M acrylamide, 0.2 M sodium acrylate, 200 µg/mL bis-acrylamide, PBS (1×), 2 mg/ml APS, 2 mg/ml TEMED, and 100 µg/mL 4HT. Sections were incubated on ice, with shaking, for 30 minutes before being mounted in gelation chambers and moved to 37 °C for one hour. After gelation, excess gel was trimmed, and the gelled tissue was recovered in pure water. With three one-hour washes in pure water, the slices expanded ~2× without disruption or cracks. These sections were moved to a 6-well glass bottom plate (Cellvis

#P06-1.5H-N, Mountain View, CA). To flatten and immobilize the sections, 4 dabs of silicon grease were applied around each section and a 22×22 mm square #2 coverslip (Corning #2855-22, Corning, NY) was pressed from above. If needed, poly-L-lysine 0.2 mg/mL (Sigma #P1524-25MG) with Photo-Flo 200 (1:500 from stock; #74257 Electron Microscopy Sciences, Hatfield, PA) were applied to the bottom of the well before the sections are placed to better immobilize the gels.

Whole-brain imaging. For high throughput imaging of 6-20 coronal sections of tens of animals (*i.e.*, hundreds of sections) we used a high-speed confocal slide scanner, equipped with a TissueFAXS 200 slide feeder (Tissuegnostics, Germany) and a SpectraX light engine (Lumencor) with the following center wavelength, power, excitation filters center, and filter width: (1) 395 nm, 400 mW (395 nm / 25 nm); (2) 475 nm, 480 mW (475 nm / 34 nm); (3) lightpipe (585 nm / 35 nm); (4) 619 nm, 629 mW (635 nm / 22 nm). These were delivered by a lightguide to a Crest X-Light V2 confocal spinning disc microscope (Crestoptics; 60 μm pinhole spinning disk) with the following dichroics from Chroma Technology: T425lpxr, T495lpxt, T600lpxr, T660lpxr and emission filters: ET460 nm / 50 nm, ET525 nm / 50 nm, ET625 nm / 30 nm, ET700 nm / 75 nm. The emission light was collected with Zeiss objectives: EC Plan-Neofluar 2.5x/0.085 M27 for tissue detection, EC Plan-Neofluar 10×/0.3 M27 for MeCP2 and PSD95 animals (**Fig. 2c–k; Extended Data Fig. 4; Supplementary Fig. 3,6**) and a Plan-Apochromat 20×/0.8 M27 for virally injected animals (**Extended Data Fig. 3; Supplementary Fig. 1,2,4**). Detection was performed using a Zyla 5.5 sCMOS camera (Andor). The acquisition of the coronal sections was carried out after semi-automated tissue detection and by using multiple autofocusing points per section (5×5 and 3×3 grids for objective acquisitions of 20× and

10× accordingly). For virally transfected animals, three z-planes were imaged and z-projected with a 7 µm spacing. For MeCP2 and PSD95 animals, a single plane was imaged.

High-resolution synaptic imaging. To segment individual nuclei of MeCP2–HaloTag-expressing cells (**Fig. 1c–f**; **Extended Data Fig. 5**) or single synapses expressing PSD95–HaloTag (**Fig. 2l**), higher resolution imaging was needed. For MeCP2 imaging we used a Zeiss LSM 880 (Blackwood, NJ) with an EC Plan-Neoflour 40×/1.3NA oil objective and a voxel size of 0.25x0.25x0.5 µm. We acquired 21 z-planes and 5 channels in 3 tracks. Detection [excitation] wavelengths were as follows (all in nm): Track 1 - DAPI: 410-489 [405]- DAPI, JF_{612}: 624-668 [594]; Track 2 IF: 493-551 [488], JF_{669}: 680-758 [633]; Track 3 JF_{552}: 553-588 [561]. For PSD95 imaging we used a Zeiss LSM 980 with Airyscan and a C-Apochromat 40×/1.2 water dipping objective after 2× expansion. The resulting pixel size after Airyscan processing was 57×57×230 nm. We acquired 23 z-sections with two channels, 561 nm illumination for JF_{552} and 633 nm illumination for JFX_{673}. A full z-stack was acquired for the far-red channel followed by the red channel.

Image analysis for dye screening. We determined the amount of saturation for each dye injected *in vivo* (**Extended Data Fig. 3; Supplementary Note 2**). Saturation must consider the amount of total protein (total = *Pulse*+*Chase*), so the *Fraction Pulse* was used as a measure of saturation: *Fraction Pulse* = *Pulse*/(*Pulse*+*Chase*). Doing a pixel-wise analysis would not be sufficient, as background can change depending on the imaged channel and brain region. We performed a mask-based analysis for the cells with a local background estimation. To set masks, we imported 2× downsampled images with 3 channels (GFP/*Pulse*/*Chase*) into Ilastik's pixel classification workflow[62]. The workflow was manually trained to segment cell bodies, dendrites, several types of neuropil signal, and different imaging and tissue artifacts. The pixel probability

maps for cells, combined with the raw data, were then imported to a second object-classification workflow in Ilastik. This workflow was used to classify each mask as a GFP–HaloTag-expressing or –negative cell. A Matlab (Mathworks) script was used to calculate the value of each mask in the three channels and to calculate a local background. The local background estimation excluded pixels that belonged to other non-neuropil trained categories (other cells, dendrites, etc.) from the first Ilastik workflow (**Extended Data Fig. 3c**). For each mask, a background subtracted value was calculated for each dye and converted to µM dye concentration using an independent calibration obtained under the same imaging conditions (**Supplemental Note 2**). *Fraction Pulse* was calculated after conversion to µM dye, where *Fraction Pulse* values closer to 1 indicate saturation.

Image analysis for MeCP2. To segment MeCP2-HaloTag nuclei and categorize them into cell types using immunofluorescence (IF), a modified Ilastik classification pipeline was used (**Fig. 1d,e; Extended Data Fig. 5**). First, the five imaged channels (DAPI, *Pulse*, *Chase1*, *Chase2*, IF) were each normalized from 0 to 1 using the top and bottom 0.3 % of the histogram. Second, a mean of all three imaged JF dyes was used to make a 3-channel image (DAPI, mean of all JF dyes, IF). This was used in the Ilastik pixel classification workflow. We used training data from all three types of IF used (NeuN, Iba1, and SOX10). The resulting nuclei probability maps in combination with the 3-channel images were used by three independent object classification workflows in Ilastik, one for each IF type. The output of these three workflows was a set of masks indicating IF-positive nuclei for each cell type. We calculated three *Fraction Pulses* from these dual Chase experiments: (1) *Pulse* / *Pulse* + *Chase 1*; (2) *Pulse* + *Chase 1* / *Pulse* + *Chase 1* + *Chase 2*; (3) *Chase 1* / *Chase 1* + *Chase 2*. We then pooled all 15 measurement (5 animals ×

3 *Fraction Pulses*) and used bootstrapping to fit a lifetime with the assumption of a single exponential decay.

Image analysis for PSD95. To assign PSD95 lifetimes across the brain, we performed a pixel-based analysis (**Fig. 2b–k**), as there is no way to segment individual puncta (synapses) without enhancing resolution, as described below (Expansion Microscopy). As with MeCP2, we converted our images to 3-channel images (DAPI/*Pulse*/*Chase*) after 2× down sampling and normalization to saturate the 0.3% top and bottom of each channel's histogram. These were then imported to an Ilastik pixel-classification workflow that was trained to detect places where synapses are a meaningful signal (*i.e.*, excluding non-tissue, artifacts, ventricles). The result was used as a mask on the original data. As in MeCP2 analysis, each pixel was converted to a lifetime estimate with the assumption of a single exponential decay after conversion to μM dye concentration using calibration curves imaged under the same conditions.

Expansion Microscopy. After acquisition using the Airyscan detector array, we used Zen Blue software (Zeiss) to process the images using a 3D reconstruction of each channel with automated deconvolution strength. The Airyscan-processed images were registered across channels as they were acquired sequentially. Shifts between channels were under three pixels. The resulting 2-channel image was normalized and used as input to an Ilastik pixel classification pipeline trained to separate synapses from the background. The resulting probability images with the normalized data were used in a second Ilastik object segmentation pipeline. Here synapses were classified as simple (single line) or complex (rings, multiple curves). Both classes were used (**Fig. 2l**). As we had segmented objects, we subtracted a local background, used a calibration to convert the values to μM dye, and obtained an estimated lifetime assuming a single exponential decay.

Alignment to the Allen CCF. To align both MeCP2 and PSD95 lifetime measurements with the Allen CCF[47], a two-step procedure was used. First, a down-sampled 24-bit RGB image of each section was generated. It was loaded with QuickNII[63] and aligned with CCF v3 at a resolution of 25 µm. This accounted for the cutting angle, a global scaling factor in the dorsoventral and mediolateral axes, and the anteroposterior location of each section. QuickNII output was used for a manual non-rigid alignment with VisuAlign[64]. The main markers for alignment were the edges of the section, the ventricles, and the fiber tracks. The VisuAlign output was another RGB image in which each color was assigned to an Allen CCF v3 id. These images were loaded and interpolated to the original size of each section, allowing the assignment of each MeCP2 nucleus and PSD95 pixel to a CCF id. As the PSD95 analysis was pixel based, we excluded any pixel belonging to the root or any part of the CCF tree under fiber tracks or ventricular system.

Dye clearance. Cranial windows were made on Anterior lateral motor cortex or primary visual cortex (centered on - 2.5 mm lateral, + 0.5 mm anterior from lambda) and a headbar was attached posterior to the window as previously described[65]. The animals were anesthetized in 1% isoflurane and kept at 37 °C with a heating pad. The optical setup was the same as previously described[66], with a custom wide-field fluorescence microscope (Thorlabs) and a sCMOS camera (Hamamatsu Orca Flash 4.0 v3). Details of illumination, objectives, and filters are presented in **Supplementary Table 1**. A baseline image was acquired before dye injection. Both the baseline and subsequent timepoints were acquired as movies of 40–50 frames at 5 Hz. This was done to reduce the chances of saturating pixels on the camera at the peak on the injection while still being above electrical noise under baseline conditions. After the estimation of the baseline, the animal was removed from head fixation and injected with dye. After dye injection, it was quickly

returned to head fixation; the field of view was compared to a baseline image under room lights and then imaged for up to four hours in intervals of 2 minutes to 20 minutes to cover the fast decay part of the dye clearance. The animal was then recovered and reimaged for up to 24 h at 4–12 h intervals.

The images were analyzed using a custom Matlab script. Briefly, each movie was averaged, and a manual ROI was defined (**Extended Data Fig. 1b**). The pixel-averaged mean was fitted to a double exponential: $F = \boldsymbol{a} * \boldsymbol{e}^{-1/\tau_1} + \boldsymbol{b} * \boldsymbol{e}^{-1/\tau_2} + \boldsymbol{c}$. Population averages were computed by binning all twelve experiments together. In cases where the injection phase was captured, an offset was used to start the fitting from the highest time point.

Carotid artery dye infusion. To measure the infusion kinetics of JF dyes, we needed a way to control the rate of infusion while imaging dye accumulation in the brain through a cranial window (**Supplemental Note 3**). We used two C57Bl/6j animals with common carotid artery vascular catheterization. These were ordered from Charles Rivers as a surgical service. They were flushed with saline and 50% sucrose lock solution every 7 days. A cranial window was performed 7 days after catheterization as described above. 7 days after cranial window surgery, a pump with JF dye was connected to the carotid artery line. The initial pump rate was 20 µl/min followed by 40 µl/min and 80 µl/min. The imaging conditions were the same as for the dye clearance experiments (0.2 s exposure) but imaged continuously for each injection speed. Data were time averaged at 1 s (5 timepoints) and a manual ROI was drawn. The time-averaged fluorescence values were trimmed to the times the pump was running and fit with a linear fit (including intercept). The values reported are the slopes of the fit.

Modeling the effects of dye clearance on saturation. Given our results on dye infusion (**Supplementary Note 3**), we wanted to test the hypothesis that given a fixed amount of dye to

inject, faster injections would lead to more dye captured in the brain. We considered a simple model where a single position in space (x position 1) is a blood vessel from which dye can enter the system and diffuse in 1D simulated by a time march (using Fourier's equation). To avoid edge conditions (Dirichlet boundary conditions were simulated) care was taken to simulate all relevant dye diffusion away from the edge. Both dye injection and clearance were simulated at the same arbitrary rate (dt). All simulations had the same total amount of dye injected, and a constant amount of dye was cleared from the vessel at a rate of 1AU/dt. Different simulations had different injection rates (2–10 AU/dt) and the width of the dye distribution was measured as the width in dx at 90% of the known saturation value.

Modeling protein turnover measurements with DELTA. Pulse-chase experiments were modeled using the SimBiology package in Matlab (**Supplementary Note 1**). Briefly, time constants of the target HaloTag fusion protein synthesis was simulated. Each new protein could either degrade (at the same rate of synthesis modeled) or attach to a HaloTag ligand dye molecule (*Pulse* or *Chase*, dye collectively). The dye binding kinetics were set to be nearly instantaneous, as they are several orders of magnitude higher than those for synthesis/degradation. Binding kinetics were identical for both the Pulse and Chase. The degradation rates of the HaloTag protein with dye complexes were the same as for the protein alone.

The dye injection kinetics were neglected (*i.e.*, instantaneous injection). Dye clearance kinetics were modeled as two compartments (named cytosol & lipids) with degradation from the cytosol compartment. This was done to account for the multiexponential decay measured *in vivo*. The cytosol compartment was set to have a volume of 1 ml; the equilibrium constant between the compartments, the volume of the lipids compartment and the degradation time constant were

fitted using the JF-dyes clearance data (**Extended Data Fig. 1**). This fitting was done in the absence of a HaloTag-protein.

Dye solubility. Formulations for the solubility measurements of the JF dyes were prepared in the following manner. (i) 30% Captisol formulation was made with 300 mg Captisol® (β-cyclodextrin sulfobutyl ethers, sodium salts; NC-04A-180186, Cydex Pharmaceuticals) dissolved in 1 mL of sterile water (Molecular Biology Grade Water, Corning) to make a 30% solution. 100 µL of this solution was added to 100 nmol of dry JF dye. (ii) A 30% (v/v) Captisol + Pluronic formulation was made by mixing a 30% Captisol solution with Pluronic F-127 (P3000MP, Invitrogen) in an 80:20 ratio. 100 µL of the prepared solution was added to 100 nmol of JF dye. (iii) The DMSO + Pluronic formulation was made with DMSO (D2650, Sigma Aldrich), Pluronic F-127, and sterile saline (0.9 % sodium chloride) mixed in a 20:20:60 (v/v/v) ratio. 100 µL from the prepared solution was added to 100 nmol of JF dye. (iv) A DMSO-only formulation was made by adding 100 µL of DMSO to 100 nmol of JF dye to bring it to a final concentration of 1 mM.

The prepared JF dye formulations were briefly vortexed followed by bath sonication (Branson 1200 model) for 5 minutes. The dye solutions were placed on the agitator for 72 h to ensure solubilization. Absorbance measurements of dye solutions were performed using a spectrometer (Cary 100 UV-Vis, Agilent Technologies), and the final concentration was determined from known extinction coefficients of JF dyes as defined by Grimm et al.[37–39].

Data and Code availability. Both metadata and raw data are available through the Open Science Foundation project associated with this paper (https://osf.io/wprhu/). The protocols are available as a collection on protocols.io. The code used for the analysis is available on GitHub.

REFERENCES

1. Price, J. C., Guan, S., Burlingame, A., Prusiner, S. B. & Ghaemmaghami, S. Analysis of proteome dynamics in the mouse brain. *Proc. Natl. Acad. Sci.* **107**, 14508–14513 (2010).
2. Alberts, B. *et al. Essential cell biology*. (W. W. Norton & Company, 2019).
3. Cohen, L. D. *et al.* Metabolic Turnover of Synaptic Proteins: Kinetics, Interdependencies and Implications for Synaptic Maintenance. *PLoS ONE* **8**, e63191 (2013).
4. Rolfs, Z. *et al.* An atlas of protein turnover rates in mouse tissues. *Nat. Commun.* **12**, 6778 (2021).
5. Soulé, J. *et al.* Balancing Arc synthesis, mRNA decay, and proteasomal degradation: maximal protein expression triggered by rapid eye movement sleep-like bursts of muscarinic cholinergic receptor stimulation. *J. Biol. Chem.* **287**, 22354–22366 (2012).
6. Heo, S. *et al.* Identification of long-lived synaptic proteins by proteomic analysis of synaptosome protein turnover. *Proc. Natl. Acad. Sci.* **115**, E3827–E3836 (2018).
7. Alvarez-Castelao, B., Schanzenbächer, C. T., Langer, J. D. & Schuman, E. M. Cell-type-specific metabolic labeling, detection and identification of nascent proteomes in vivo. *Nat. Protoc.* **14**, 556–575 (2019).
8. Cohen, L. D. & Ziv, N. E. Neuronal and synaptic protein lifetimes. *Curr. Opin. Neurobiol.* **57**, 9–16 (2019).
9. Fornasiero, E. F. *et al.* Precisely measured protein lifetimes in the mouse brain reveal differences across tissues and subcellular fractions. *Nat. Commun.* **9**, 1–17 (2018).
10. Dörrbaum, A. R., Kochen, L., Langer, J. D. & Schuman, E. M. Local and global influences on protein turnover in neurons and glia. *eLife* **7**, e34202 (2018).
11. Paterson, R. W. *et al.* SILK studies — capturing the turnover of proteins linked to neurodegenerative diseases. *Nat. Rev. Neurol.* **15**, 419–427 (2019).

12. Flexner, J. B., Flexner, L. B. & Stellar, E. Memory in Mice as Affected by Intracerebral Puromycin. *Science* **141**, 57–59 (1963).

13. Luft, A. R., Buitrago, M. M., Ringer, T., Dichgans, J. & Schulz, J. B. Motor Skill Learning Depends on Protein Synthesis in Motor Cortex after Training. *J. Neurosci*. **24**, 6515–6520 (2004).

14. Park, H. & Kaang, B.-K. Balanced actions of protein synthesis and degradation in memory formation. *Learn. Mem.* **26**, 299–306 (2019).

15. Kelleher, R. J., Govindarajan, A., Jung, H.-Y., Kang, H. & Tonegawa, S. Translational Control by MAPK Signaling in Long-Term Synaptic Plasticity and Memory. *Cell* **116**, 467–479 (2004).

16. McGaugh, J. L. Memory--a Century of Consolidation. *Science* **287**, 248–251 (2000).

17. Fioravante, D. & Byrne, J. H. Protein degradation and memory formation. *Brain Res. Bull.* **85**, 14–20 (2011).

18. Fonseca, R., Vabulas, R. M., Hartl, F. U., Bonhoeffer, T. & Nägerl, U. V. A Balance of Protein Synthesis and Proteasome-Dependent Degradation Determines the Maintenance of LTP. *Neuron* **52**, 239–245 (2006).

19. Lee, S.-H. *et al*. Synaptic Protein Degradation Underlies Destabilization of Retrieved Fear Memory. *Science* **319**, 1253–1256 (2008).

20. DeNardo, L. A. *et al.* Temporal evolution of cortical ensembles promoting remote memory retrieval. *Nat. Neurosci.* **22**, 460–469 (2019).

21. Roy, D. S. *et al*. Brain-wide mapping reveals that engrams for a single memory are distributed across multiple brain regions. *Nat. Commun.* **13**, 1799 (2022).

22. Ye, L. *et al*. Wiring and Molecular Features of Prefrontal Ensembles Representing Distinct Experiences. *Cell* **165**, 1776–1788 (2016).

23. Bliss, T. V. & Lomo, T. Long-lasting potentiation of synaptic transmission in the dentate area of the anaesthetized rabbit following stimulation of the perforant path. *J. Physiol.* **232**, 331–356 (1973).

24. Frey, U. & Morris, R. G. M. Synaptic tagging and long-term potentiation. *Nature* **385**, 533–536 (1997).

25. Harvey, C. D. & Svoboda, K. Locally dynamic synaptic learning rules in pyramidal neuron dendrites. *Nature* **450**, 1195–1200 (2007).

26. Matsuzaki, M., Honkura, N., Ellis-Davies, G. C. R. & Kasai, H. Structural basis of long-term potentiation in single dendritic spines. *Nature* **429**, 761–766 (2004).

27. Nabavi, S. *et al.* Engineering a memory with LTD and LTP. *Nature* **511**, 348–352 (2014).

28. Chen, X., Wei, S., Ji, Y., Guo, X. & Yang, F. Quantitative proteomics using SILAC: Principles, applications, and developments. *PROTEOMICS* **15**, 3175–3192 (2015).

29. Alvarez-Castelao, B. & Schuman, E. M. The Regulation of Synaptic Protein Turnover. *J. Biol. Chem.* **290**, 28623–28630 (2015).

30. Butko, M. T. *et al.* Fluorescent and photo-oxidizing TimeSTAMP tags track protein fates in light and electron microscopy. *Nat. Neurosci.* **15**, 1742–1751 (2012).

31. Lin, M. Z., Glenn, J. S. & Tsien, R. Y. A drug-controllable tag for visualizing newly synthesized proteins in cells and whole animals. *Proc. Natl. Acad. Sci.* **105**, 7744–7749 (2008).

32. Keppler, A. *et al.* A general method for the covalent labeling of fusion proteins with small molecules in vivo. *Nat. Biotechnol.* **21**, 86–89 (2003).

33. Bojkowska, K. *et al.* Measuring In Vivo Protein Half-Life. *Chem. Biol.* **18**, 805–815 (2011).

34. Hawkins, B. T. & Egleton, R. D. Fluorescence imaging of blood-brain barrier disruption. *J. Neurosci. Methods* **151**, 262–267 (2006).

35. Los, G. V. *et al.* HaloTag: a novel protein labeling technology for cell imaging and protein analysis. *ACS Chem. Biol.* **3**, 373–382 (2008).

36. Bulovaite, E. *et al.* A brain atlas of synapse protein lifetime across the mouse lifespan. *Neuron* (2022) doi:10.1016/j.neuron.2022.09.009.

37. Grimm, J. B. *et al.* A general method to fine-tune fluorophores for live-cell and in vivo imaging. *Nat. Methods* **14**, 987–994 (2017).

38. Grimm, J. B. *et al.* A general method to optimize and functionalize red-shifted rhodamine dyes. *Nat. Methods* **17**, 815–821 (2020).

39. Grimm, J. B. *et al.* A General Method to Improve Fluorophores Using Deuterated Auxochromes. *JACS Au* **1**, 690–696 (2021).

40. Lavis, L. D. What if we just give everything away? *eLife* **10**, e74981 (2021).

41. Verkhusha, V. V. *et al.* High Stability of Discosoma DsRed As Compared to Aequorea EGFP. *Biochemistry* **42**, 7879–7884 (2003).

42. Ehrhart, F. *et al.* Rett syndrome – biological pathways leading from MECP2 to disorder phenotypes. *Orphanet J. Rare Dis.* **11**, (2016).

43. Qiu, Z. *et al.* The Rett Syndrome Protein MeCP2 Regulates Synaptic Scaling. *J. Neurosci.* **32**, 989–994 (2012).

44. Zimmermann, C. A., Hoffmann, A., Raabe, F. & Spengler, D. Role of Mecp2 in Experience-Dependent Epigenetic Programming. *Genes* **6**, 60–86 (2015).

45. Piccolo, F. M. *et al.* MeCP2 nuclear dynamics in live neurons results from low and high affinity chromatin interactions. *eLife* **8**, e51449 (2019).

46. Mecp2 protein abundance - PAXdb. https://pax-db.org/protein/5020631.

47. Wang, Q. *et al.* The Allen Mouse Brain Common Coordinate Framework: A 3D Reference Atlas. *Cell* **181**, 936-953.e20 (2020).

48. Shahbazian, M. D., Antalffy, B., Armstrong, D. L. & Zoghbi, H. Y. Insight into Rett syndrome: MeCP2 levels display tissue- and cell-specific differences and correlate with neuronal maturation. *Hum. Mol. Genet.* **11**, 115–124 (2002).

49. Cho, K.-O., Hunt, C. A. & Kennedy, M. B. The rat brain postsynaptic density fraction contains a homolog of the drosophila discs-large tumor suppressor protein. *Neuron* **9**, 929–942 (1992).

50. Masch, J.-M. *et al.* Robust nanoscopy of a synaptic protein in living mice by organic-fluorophore labeling. *Proc. Natl. Acad. Sci.* **115**, E8047–E8056 (2018).

51. Nithianantharajah, J. & Hannan, A. J. Enriched environments, experience-dependent plasticity and disorders of the nervous system. *Nat. Rev. Neurosci.* **7**, 697–709 (2006).

52. Rosenzweig, M. R. & Bennett, E. L. Effects of differential environments on brain weights and enzyme activities in gerbils, rats, and mice. *Dev. Psychobiol.* **2**, 87–95 (1969).

53. Zhang, X. *et al.* High-resolution mapping of brain vasculature and its impairment in the hippocampus of Alzheimer's disease mice. *Natl. Sci. Rev.* **6**, 1223–1238 (2019).

54. Chen, F., Tillberg, P. W. & Boyden, E. S. Expansion microscopy. *Science* **347**, 543–548 (2015).

55. Tillberg, P. W. *et al.* Protein-retention expansion microscopy of cells and tissues labeled using standard fluorescent proteins and antibodies. *Nat. Biotechnol.* **34**, 987–992 (2016).

56. Huff, J. The Airyscan detector from ZEISS: confocal imaging with improved signal-to-noise ratio and super-resolution. *Nat. Methods* **12**, i–ii (2015).

57. Wang, Y. *et al.* EASI-FISH for thick tissue defines lateral hypothalamus spatio-molecular organization. *Cell* **184**, 6361-6377.e24 (2021).

58. Ld, C., A, B. & Ne, Z. A non-fluorescent HaloTag blocker for improved measurement and visualization of protein synthesis in living cells. *F1000Research* **9**, (2020).

59. Merrill, R. A. *et al.* A robust and economical pulse-chase protocol to measure the turnover of HaloTag fusion proteins. *J. Biol. Chem.* **294**, 16164–16171 (2019).

60. Damstra, H. G. *et al.* Visualizing cellular and tissue ultrastructure using Ten-fold Robust Expansion Microscopy (TREx). *eLife* **11**, e73775 (2022).

61. Chan, K. Y. *et al.* Engineered AAVs for efficient noninvasive gene delivery to the central and peripheral nervous systems. *Nat. Neurosci.* **20**, 1172–1179 (2017).

62. Berg, S. *et al.* ilastik: interactive machine learning for (bio)image analysis. *Nat. Methods* **16**, 1226–1232 (2019).

63. QuickNII; RRID:SCR_016854; http://www.nitrc.org/projects/quicknii/. (2022).

64. VisuAlign; RRID:SCR_017978; http://www.nitrc.org/projects/visualign/. (2021).

65. Ashby, M. C. *et al.* Removal of AMPA Receptors (AMPARs) from Synapses Is Preceded by Transient Endocytosis of Extrasynaptic AMPARs. *J. Neurosci.* **24**, 5172–5176 (2004).

66. Abdelfattah, A. S. *et al.* Bright and photostable chemigenetic indicators for extended in vivo voltage imaging. *Science* **365**, 699–704 (2019).

67. Yardeni, T., Eckhaus, M., Morris, H. D., Huizing, M. & Hoogstraten-Miller, S. Retro-orbital injections in mice. *Lab Anim.* **40**, 155–160 (2011).

68. Holtmaat, A. *et al.* Long-term, high-resolution imaging in the mouse neocortex through a chronic cranial window. *Nat. Protoc.* **4**, 1128–1144 (2009).

69. Trachtenberg, J. T. *et al.* Long-term in vivo imaging of experience-dependent synaptic plasticity in adult cortex. *Nature* **420**, 788–794 (2002).

70. Walther, D. M. & Mann, M. Accurate Quantification of More Than 4000 Mouse Tissue Proteins Reveals Minimal Proteome Changes During Aging *. *Mol. Cell. Proteomics* **10**, S1–S7 (2011).

71. Zhao, Y., Denner, L., Haidacher, S. J., LeJeune, W. S. & Tilton, R. G. Comprehensive analysis of the mouse renal cortex using two-dimensional HPLC – tandem mass spectrometry. *Proteome Sci.* **6**, 15 (2008).

72. Caujolle, F., Caujolle, D., Bouyssou, H. & Calvet, M. M. Toxicity and pharmacological aptitudes of Dimethylsulfoxide. *Comptes Rendus Hebd. Seances Acad. Sci.* **258**, 2224–2226 (1964).

73. Krenzlin, H., Lorenz, V., Danckwardt, S., Kempski, O. & Alessandri, B. The Importance of Thrombin in Cerebral Injury and Disease. *Int. J. Mol. Sci.* **17**, 84 (2016).

ACKNOWLEDGMENTS

We would like to thank the following Janelia shared support team members. Histology: Benjamin Foster, Monique Copeland, Amy Hu, Susan Michael; Imaging: Michael DeSantis, Damien Alcor; Vivarium: Gillian Harris, Mariam Rose, Sarah Lindo; Viruses: Alina Gutu, Kim Ritola, Hyuh Ah Yi; Tool Translation Team: Ariana Tkachuk; Open chemistry: Anastasia Osowski, Katie Holland. We thank Eric Schreiter for the GFP-HaloTag virus, James Liu for the

MeCP2-HaloTag animal, and Seth Grant for the PSD95-HaloTag animal. We also thank Amrita Singh for assistance with dye clearance imaging.

FIGURES

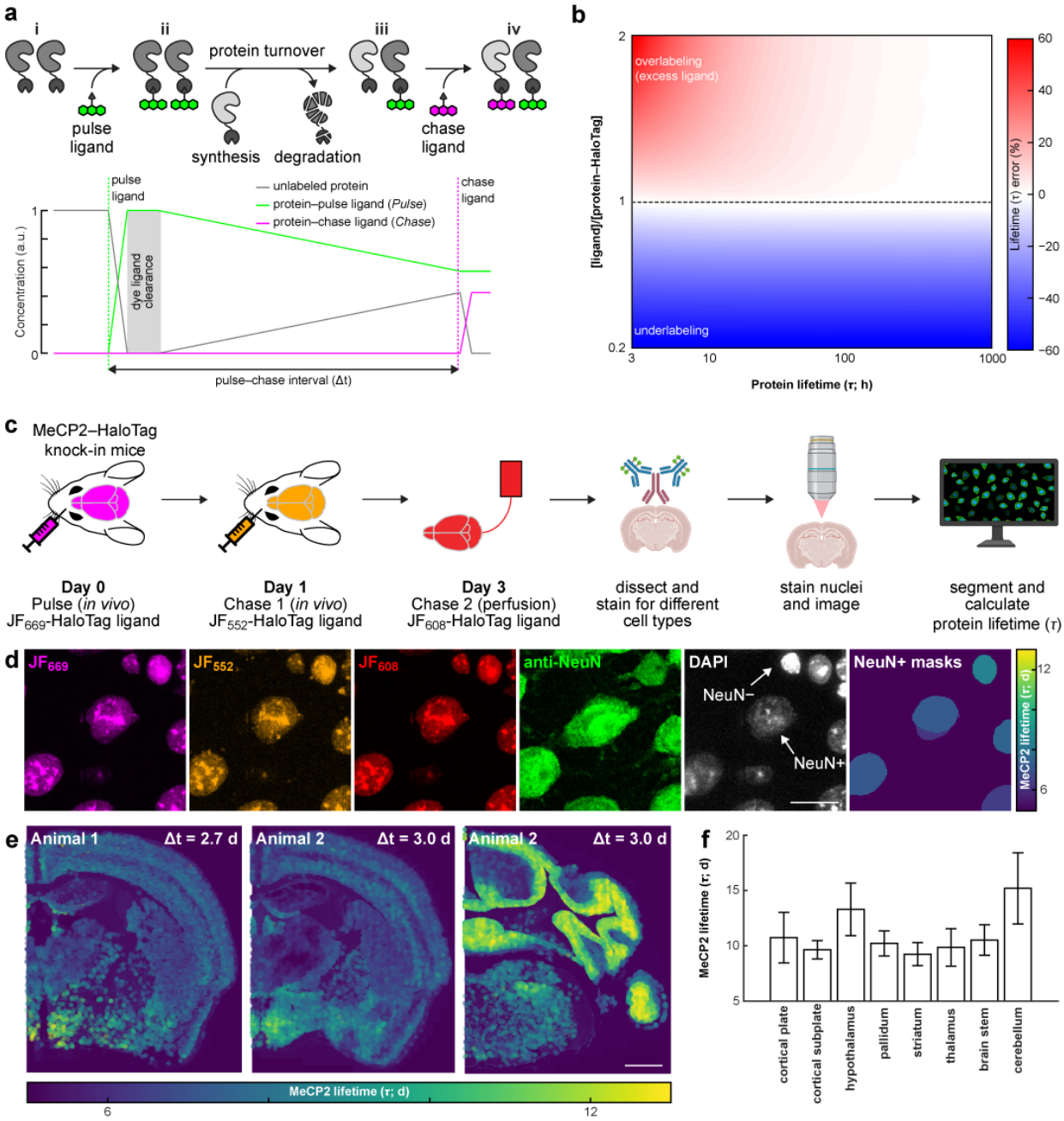

Figure 1 – Measurement of protein turnover *in vivo*, demonstrated with MeCP2.

a, Schematics showing dye capture by a protein-HaloTag fusion. (i) Before the injection of the first dye ligand, all proteins are unlabeled (gray line). (ii) After injection of the first dye

(dashed green line), all proteins are labeled with the pulse dye (solid green line - *Pulse*). (iii) During the pulse–chase interval, some proteins degrade, and others are synthesized but are unlabeled. (iv) Injection of a spectrally separate dye (dashed magenta line) binds the newly synthesized protein (solid magenta line - *Chase*). The gray shaded area indicates where excess dye delays the onset of turnover measurement, leading to a *Pulse* overestimation error. **b**, Simulation with different dye ligand to protein ratios (y-axis) and true lifetimes (x-axis). The estimated lifetime error is colored. Undersaturation (bottom half; <1 ligand/protein ratio) causes worse errors than dye excess (top half; >1 ligand/protein ratio) and longer-lived proteins are estimated more accurately than short-lived ones. **c–d,** Turnover measurement of the nuclear protein MeCP2-HaloTag in a knock-in mouse model. (c) Experimental design: Three dyes were used to measure multiple protein-turnover intervals. Additionally, after perfusion and dissection, coronal sections were labeled with DAPI and fluorescent antibodies to identify different cell types. (d) Example field-of-view showing the JF dye ligand signals (left 3 panels) with NeuN and DAPI for identification of neuronal nuclei. After segmentation of NeuN positive nuclei, segmented nuclei were colored by lifetime using the sum of the two *in vivo* injections as the pulse ($[JF_{669}+JF_{552}]/[JF_{669}+JF_{552}+JF_{608}]$). **e,** Example coronal sections from two animals. Left and middle, illustration of the consistency of the lifetime estimates for aligned AP sections; Right, longer lifetime in the cerebellum (compare to middle and left panels). **f,** MeCP2-HT lifetime means and bootstrap confidence intervals for aligned brain regions.

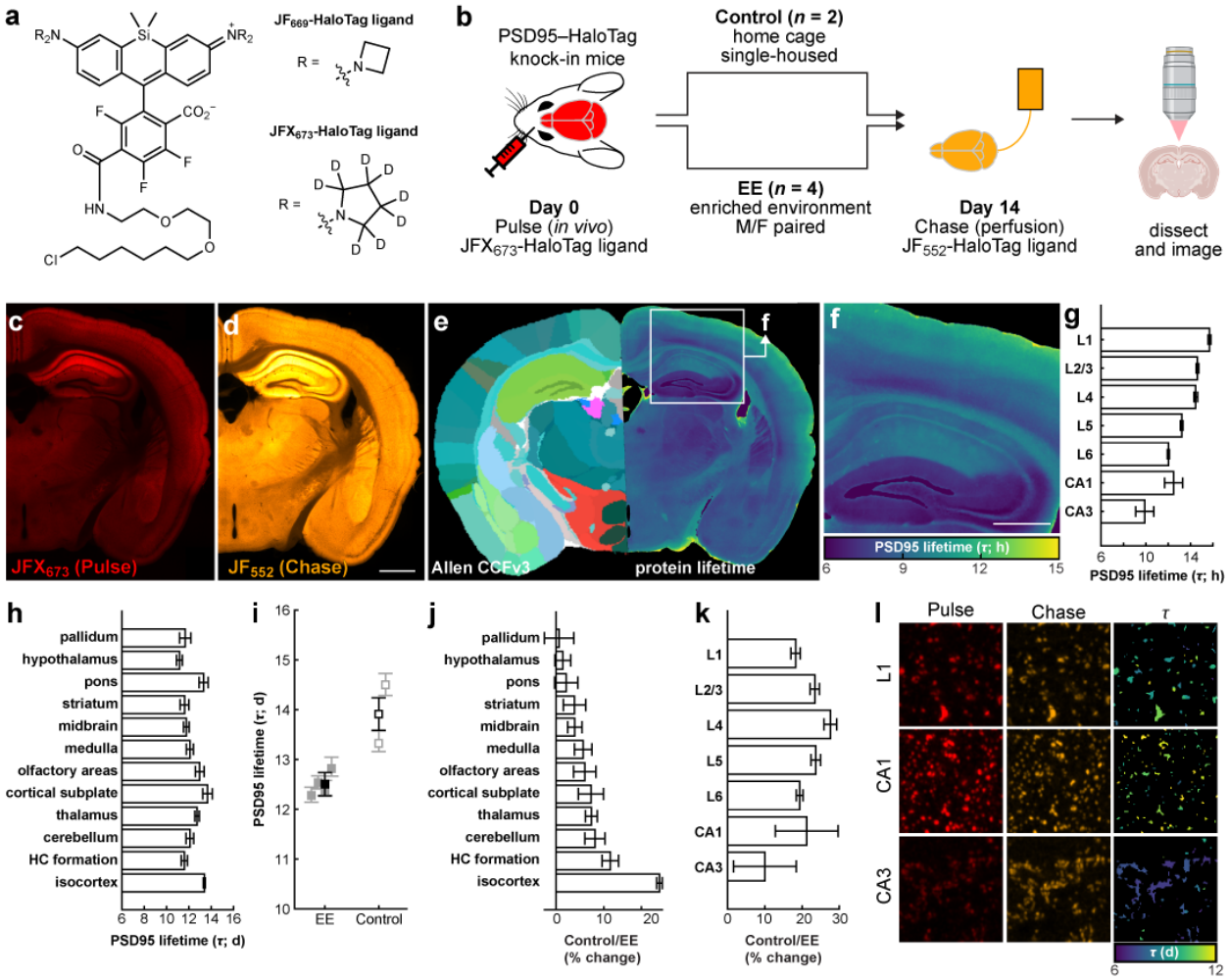

Figure 2 – PSD95 turnover depends on experience.

a, Structure of JF_{669}-HaloTag ligand and deuterated JFX_{673}-HaloTag ligand. **b,** Experimental design for turnover measurement of PSD95-HaloTag in a knock-in mouse. See text for details. **c–e,** Example coronal section showing the pulse (**c**), chase (**d**), and calculated lifetime aligned to the Allen CCFv3 (**e**). **f,** zoom-in of the image from panel (**e**). Note the lifetime gradient that separates the CA1 *stratum radiatum* & *stratum lacunosum moleculare* (long lifetime) from dentate gyrus *stratum moleculare*, and hilus (all short lifetime). **g**, Average lifetimes of cortical layers and subfields of the hippocampus (HC) are significantly different (1-way ANOVA, df=6, F=125.09 p=5.5e-70). **h**, Average lifetime for twelve large brain regions is also significantly

different (1-way ANOVA, df=11, F=1494, p=7.6e-25). **i,** Average lifetime of four mice under EE (magenta) and two under Control conditions (green). EE increased protein turnover and shortened the average lifetime of PSD95. Individual animals in lighter colors (EE: 12.5±0.23 days n=4; Control, green: 13.9±0.33 days n=2; ANOVA df=1, F=12.28 p=0.0248). **j,** Percent change in Control vs. EE animals for twelve different brain regions; 1-way ANOVA, df=11, F=38.44, p=4.0e-58. **k,** same as (j) for cortical layers and HC subfields (1-way ANOVA, df=6, F=5.3 p=3.8e-5). **l,** Example images using Airyscan imaging of ExM tissue (max projection of 5 z-planes 0.3 um apart) from layer 1 (top row), HC CA1 subfield (middle row), and basal dendrites of CA3 (bottom row) showing both pulse, chase, and lifetime.

EXTENDED DATA FIGURES

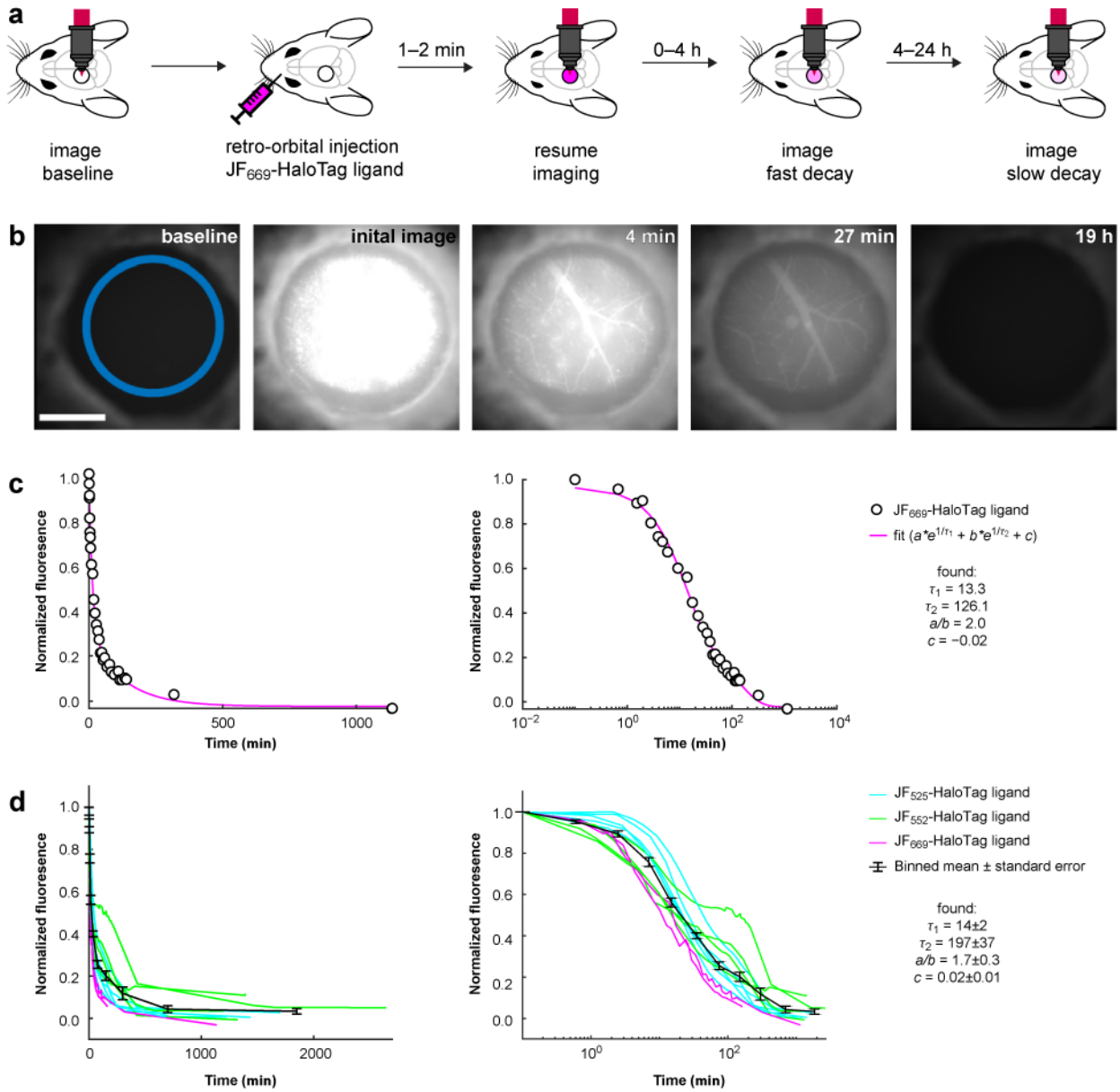

Extended Data Figure 1 - JF-HaloTag ligand dyes are cleared from the brain in hours.

a, Schematic of experimental procedure to measure dye clearance. Note that the injection kinetics are not captured as the animal is injected prior to imaging. **b,** Example images for a JF_{669}-HaloTag ligand injection. The blue circle represents the region for which fluorescence was quantified in (c). The scale bar is 2 mm. **c,** Linear (left panel) and log (right panel) scaled values

(peak normalized and baseline subtracted - blue circles) of JF_{669}-HaloTag ligand dye clearance. Double exponential fit in red; τ_1 and τ_2 are in minutes. **d,** Data from 12 experiments showing clearance of 3 dyes (JF_{525} in green, JF_{552} in red, and JF_{669} in magenta). The black trace is a binned average with standard error of all twelve experiments. The values in (**d**) represent the mean ± standard error of double exponential fits for the 12 experiments.

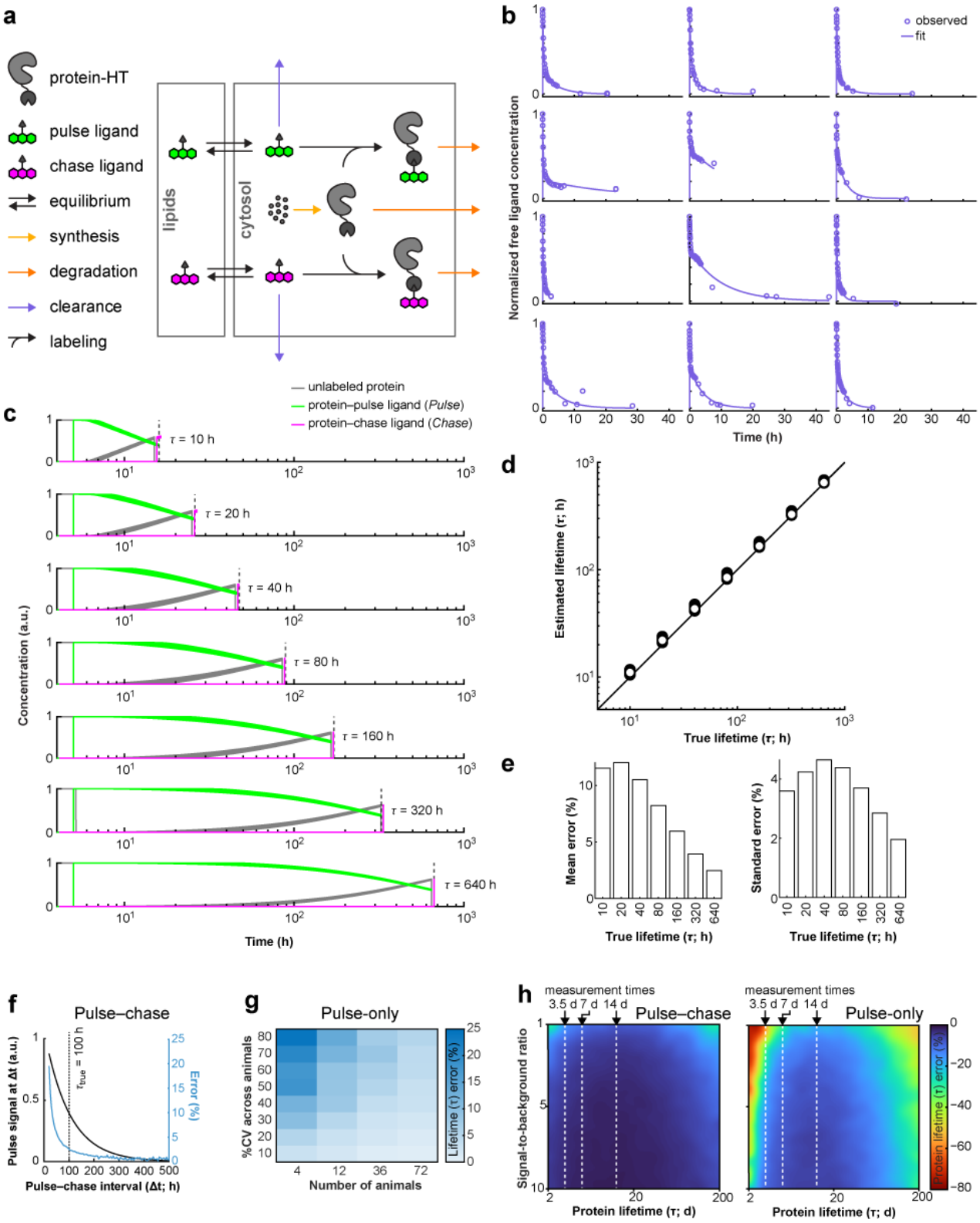
a
protein-HT
pulse ligand
chase ligand
equilibrium
synthesis
degradation
clearance
labeling
lipids
cytosol
b
observed
fit
Normalized free ligand concentration
Time (h)
c
unlabeled protein
protein–pulse ligand (Pulse)
protein–chase ligand (Chase)
τ = 10 h
τ = 20 h
τ = 40 h
τ = 80 h
τ = 160 h
τ = 320 h
τ = 640 h
Concentration (a.u.)
Time (h)
d
Estimated lifetime (τ; h)
True lifetime (τ; h)
e
Mean error (%)
Standard error (%)
True lifetime (τ; h)
f
Pulse–chase
Pulse signal at Δt (a.u.)
Error (%)
Pulse–chase interval (Δt; h)
g
Pulse-only
%CV across animals
Number of animals
Lifetime (τ) error (%)
h
measurement times
3.5 d 7 d 14 d
Pulse–chase
Pulse-only
Signal-to-background ratio
Protein lifetime (τ; d)
Protein lifetime (τ) error (%)

Extended Data Figure 2 – Modeling pulse-chase experiments *in vivo*, constrained by dye clearance measurements.

a, Model compartments, species, and reactions for modeling protein turnover measurements. A pulse or chase dye can be injected into a cytosol compartment and degrade (representing fast dye clearance) or move to a lipid compartment (representing the slow dye clearance component) or bind to the Protein. The protein synthesis rate is equal to its degradation rate, with dye-bound proteins degrading at the same rate. See **Supplementary Note 1** for more information. **b**, Fitting of the *in vivo* dye clearance data to generate model variants. 12 experiments (data in blue circles) and the fitted response (blue line) are shown. The parameters fit were dye clearance rate, brain-to-lipid equilibrium constant, and volume ratio of the lipid to cytosolic compartments. **c-e,** Example model simulations with 7 lifetimes (**c**: 10-640 h) and in each simulating all 12 variants. There is a particularly good correlation between the simulated and calculated lifetimes (**d**). The mean errors (**e**; left) are reduced as a function of lifetime, while the standard error between model variants (simulating variability in dye clearance) peaks around the mean dye clearance rate (e; right). **f**, Simulation of error in the lifetime estimate as a function of the pulse-chase interval (Δt). The error (blue line) decreases faster than the *Pulse* concentration (black line). This is in support of DELTA error being dominated by dye clearance, with overall low error rates. **g,** Error in lifetime estimation using only pulse measurements given ideal dye delivery. Here, variability of the measurement across animals (CV y-axis) could be countered only by averaging across animals (number of animals x-axis). Error rates (color-coded) are higher than in DELTA, where the chase dye and the *Fraction Pulse* calculation normalizes for inter-animal variability. **h**, Modeling to compare errors due to shot noise with DELTA (left panel) *vs.* pulse-only labeling (right panel). In both cases three measurement times (white dashed lines) were used to estimate

the known decay (x-axis: 2-200 days). Increasing the signal to background ratio (y-axis) and adding a chase dye (left panel) reduced shot-noise induced errors.

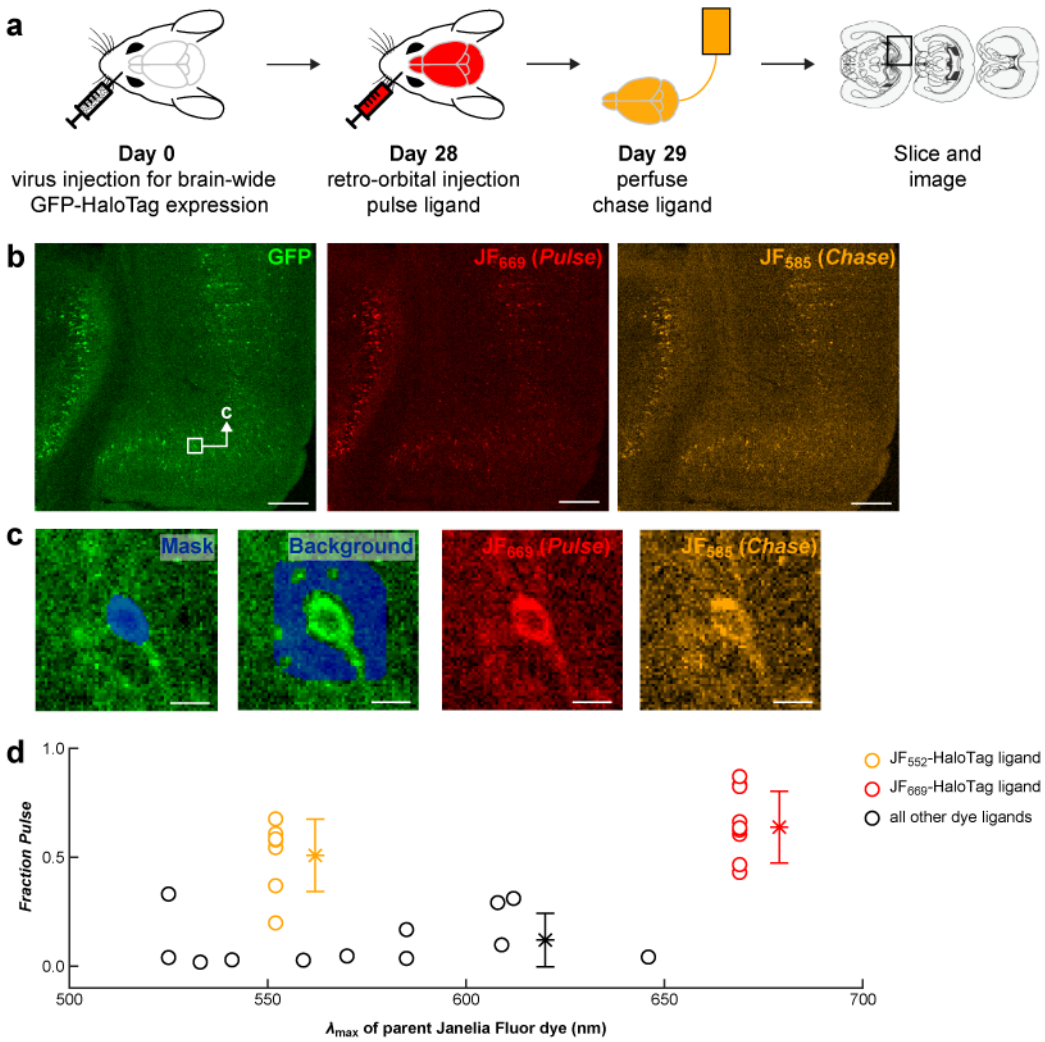

Extended Data Figure 3 – JF_{552} and JF_{669} are bioavailable in the brain.

a, Schematic of the experimental procedures for dye screening *in vivo*. **b,** Example coronal sections imaged from an animal 3 weeks after viral injection of GFP-HaloTag (left panel) where JF_{669} was injected *in vivo* (middle panel) and perfused with JF_{585}-HaloTag ligand (right panel). Scale bars, 200 µm. **c,** Example cell (square in **b**, left panel) overlaid with the mask used to extract signal (first panel), a local background (second panel) and the images of the *in vivo* injected dye (third panel) and perfused dye (fourth panel). *Fraction Pulse* is 0.65 in this example. Scale bars are 10 µm. **d,** Mean *Fraction Pulse* for each animal (n = 31) injected as a function of

the dye excitation wavelength. JF_{669}-HaloTag ligand (magenta ; n = 10, *Fraction Pulse*: 0.64 ± 0.16) and JF_{552}-HaloTag ligand (red; n = 7; *Fraction Pulse:* 0.51 ± 0.17) were significantly better than the other dyes (black; n = 14, *Fraction Pulse*: 0.12 ± 0.12; 1-way ANOVA F=35.96, df=2, p =3.2e-08; post-hoc JF_{669} vs. others p=3.8e-8, JF_{552} vs. others p=2.7e-5). Here *Fraction Pulse* was used to rank dyes by bioavailability. *Fraction Pulse* < 1.0 of a dye does not indicate the inability to saturate in other experiments.

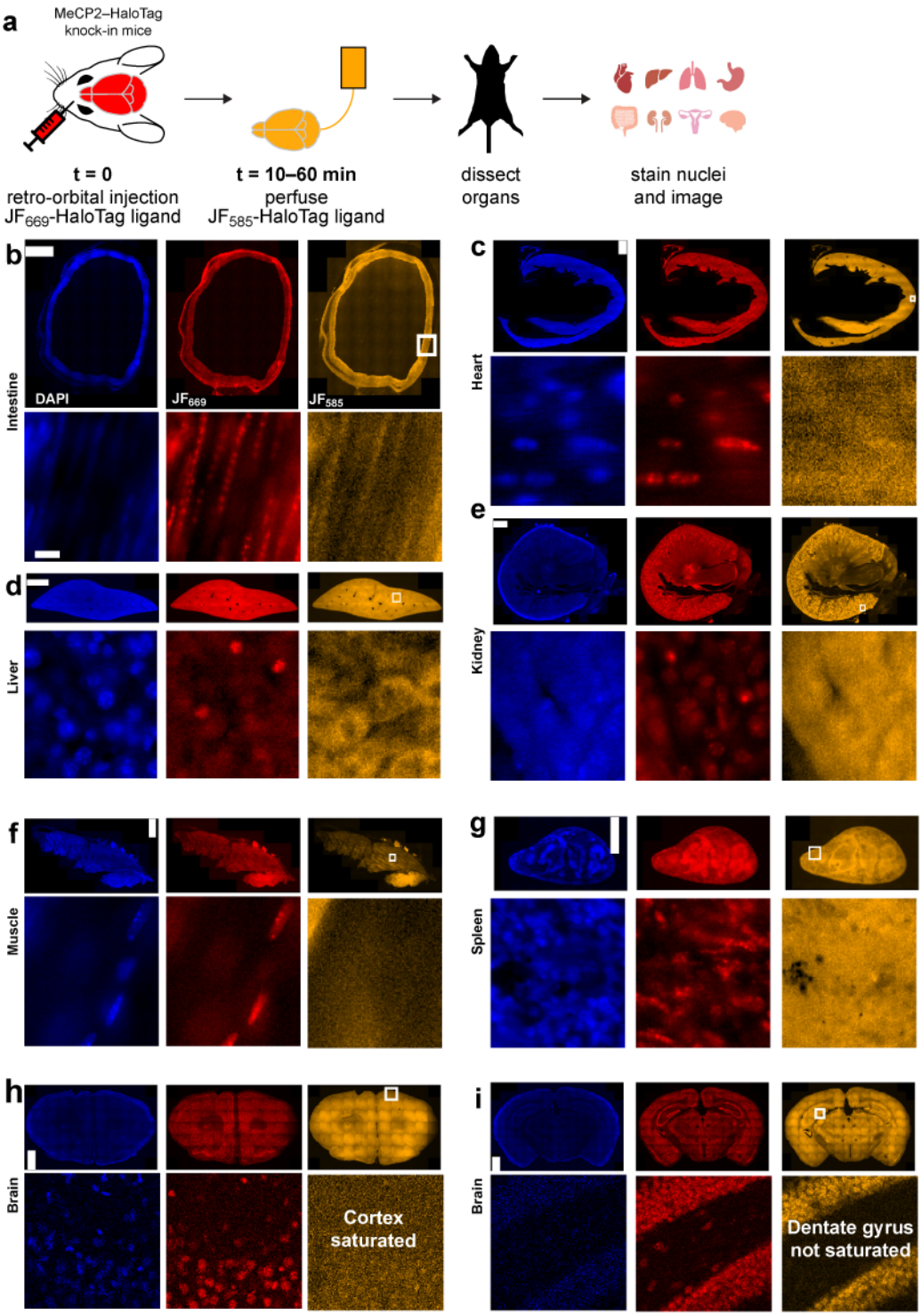

Extended Data Figure 4 – Systemic injection of ligand dye saturates the abundant protein MeCP2-HT in most organs.

a, Schematic of the experimental procedures to test the saturation of MeCP2-HT. **b-i,** Organs harvested and imaged for pulse dye saturation (red), as evident by the lack of chase dye (orange) in the nuclei (blue) where MeCP2-HT is expressed. See also **Supplemental Figure 3** for more sections of the animal in panels (h,i). Top scale bar is 1 mm, bottom scale bars are 50 μm.

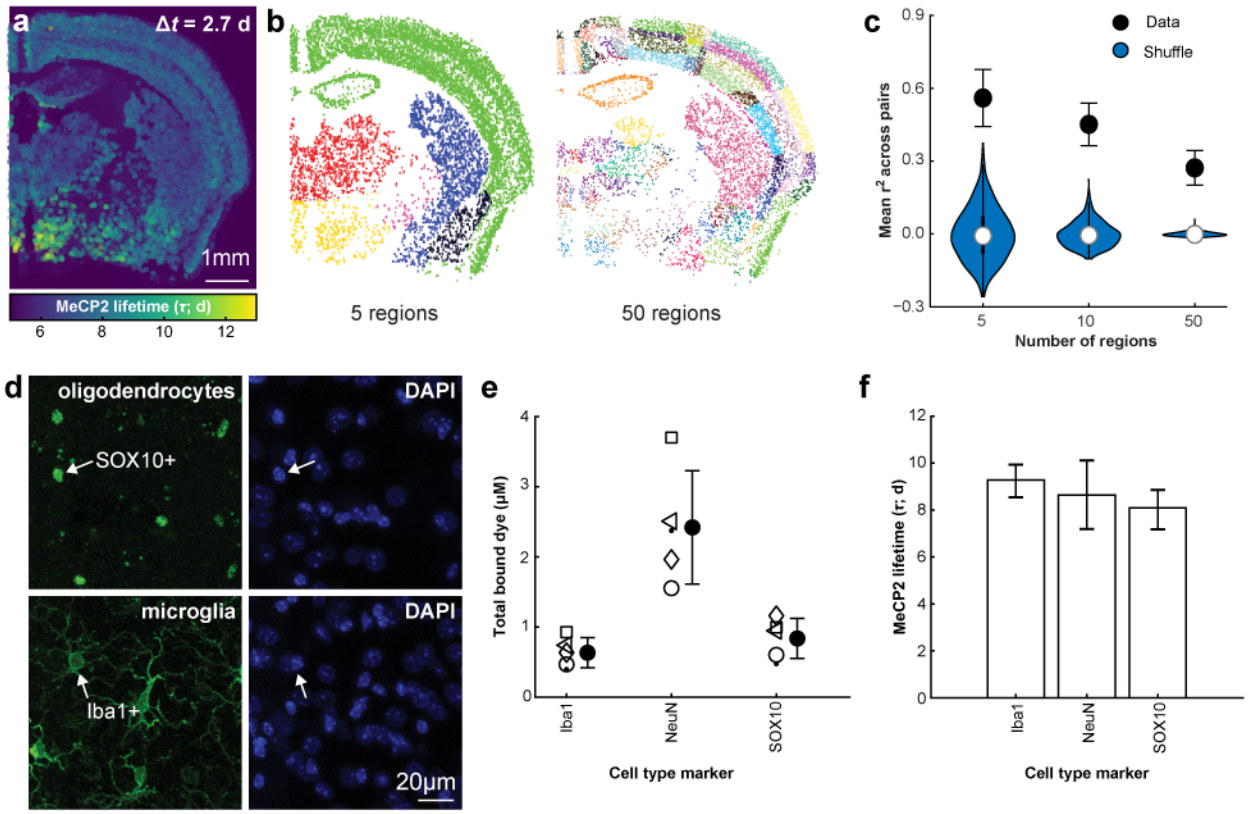

Extended Data Figure 5 – The lifetime of MeCP2-HT is consistent across individual mice and cell-types.

a, Example coronal section of the lifetime of MeCP2-HT after segmentation of positive nuclei. **b,** Example assignment of nuclei to brain regions based on the Allen CCF v3 at various levels (left 5 regions, right 50 regions). **c,** Protein lifetime measurements were consistent between mice as assessed by examining correlations between all pairs of animals (n=5 animals, 10 pairs). For three levels of the CCF (5, 10, and 50 regions) the correlation between regions was higher than for a shuffled control. **d,** Two additional sections were stained in each of the five animals for oligodendrocytes (SOX10, top) and microglia (Iba1, bottom). **e,** MeCP2 was more abundant in the nuclei of neurons (Iba1: 0.63±0.21, NeuN: 2.42±0.8 SOX10: 0.84±0.28 μM total

dye signal; ANOVA F=27.22, df=2, p=2e-4). **f,** Lifetimes were similar for all cell types, as confidence intervals overlapped between all cell types (mean and [CI] of Iba1: 9.2 [8.5, 9.9], NeuN: 8.6 [7.1 10.0], SOX10: 8.1 [7.2, 8.9] days of MeCP2 lifetime).

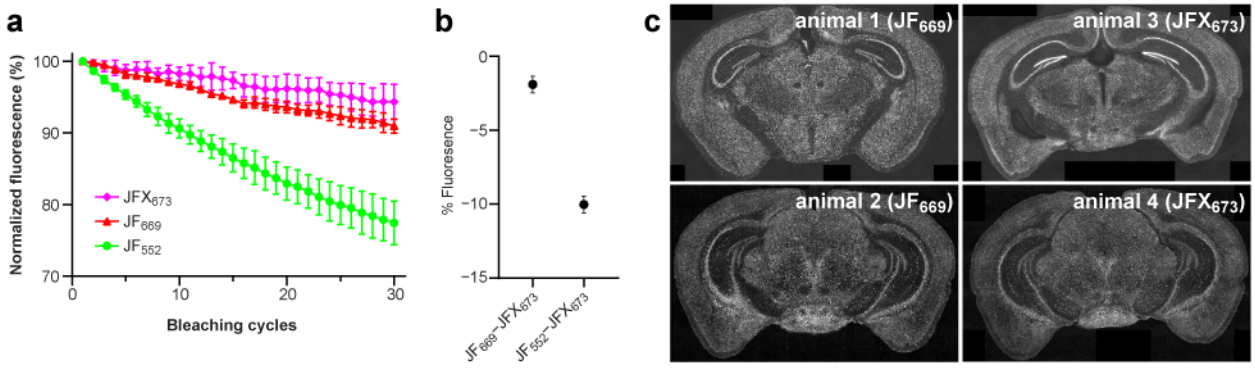

Extended Data Figure 6 – Development of JFX673-HTL for optimal in vivo dye delivery.

a, Bleaching curves of JF dyes showing normalized fluorescence over 30 bleaching cycles. **b,** JFX_{673}-HTL was significantly more photostable than the other dyes tested. **c,** Example sections of MeCP2-HT mice do not show significant differences in brain availability of JF_{669}-HTL versus JFX_{673}-HTL. All panels show the pulse dye.

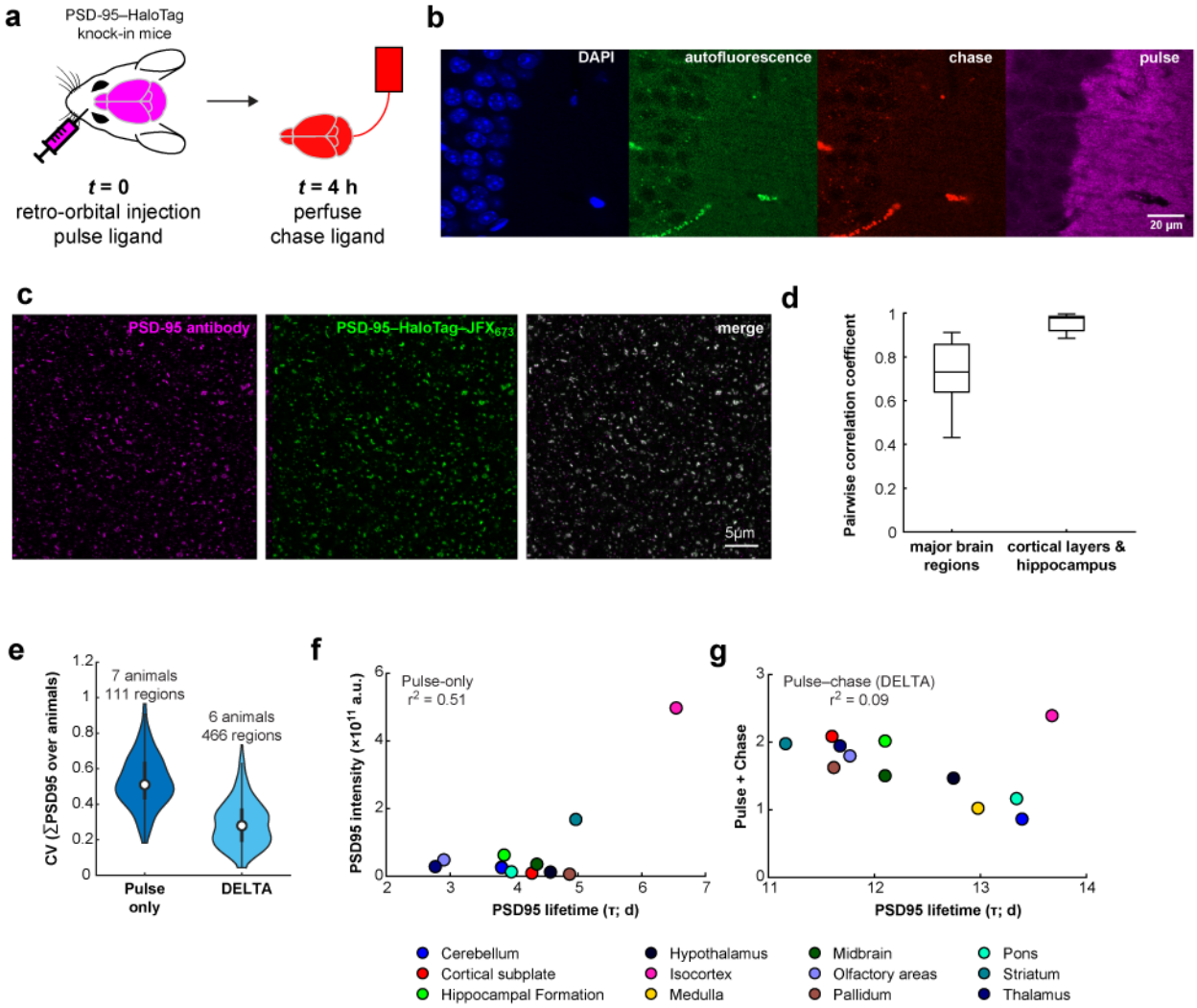

Extended Data Figure 7 – Validation of DELTA in the PSD95-HaloTag mouse.

a, Experimental procedures for testing saturation in a PSD95-HT mouse. **b** Example section showing the basal dendrite section of the CA1 region of the hippocampus (DAPI shows the nuclei in the leftmost panel). The green channel (autofluorescence; 2nd panel from left) explains all the signal in the red channel (Chase – JF_{552}-HTL; 3rd panel), while the far-red channel shows the expected pattern of synapses (Pulse – JFX_{673}-HTL; 4th panel). **c**, Validation of HTL signal (JF_{552}-HTL; middle panel) in the PSD95-HT knock-in animal with a knockout validated antibody (left panel) showing high colocalization (right panel). **d**, Box plot of all pairs of animals (6

animals, n=15 pairs) for correlation coefficients for the lifetime of PSD95 across 12 large brain regions (left) or cortical layers and HC subfields (right). **e**, Violin plot of coefficient of variation (CV) across animals for the total PSD95 measured for each brain region. Pulse only is data from Bulovaite et al. (2022) where we used the standard deviation divided by the mean of integrated fluorescence at day 0 (n=7 animals; n=111 brain regions). For DELTA we used the standard deviation divided by the mean of the total pulse and chase values (n=6 animals; n=466 brain regions). Measurement variability of total PSD95 across animals was lower in DELTA then in Bulovaite et al. (Wilcoxon rank sum test; z=12.6; p = 1.3e-36). **f-g**, Correlation between estimated expression of PSD95 (y axis) with its lifetime measurement (x axis) from publicly available data of Bulovaite et al. (f; Pulse only) or from DELTA (g) for twelve brain regions (colored circles). r^2 values from linear regression are shown for each panel.